CAS A: THE BRIGHT X-RAY KNOTS AND OXYGEN EMISSION

D. Dewey, T. DeLaney, and J.S. Lazendic²

RESUMEN

Favor de proporcionar un resumen en español. If you cannot provide a spanish abstract, the editors will do this. Chandra High-Energy Transmission Grating (HETG) X-ray spectra are extracted from 17 bright, narrow regions of Cas A and provide unique measurements of their kinematic and plasma states. From the dominant emission lines, e.g. He-like Si, we derive accurate Doppler shifts in the range -2500 to $+4000 \text{ km s}^{-1}$; these agree well with transverse-velocity measurements and allow the features to be located in 3D. Plasma diagnostics of these regions indicate temperatures largely around 1 keV with some above 3 keV. Using as well the non-dispersed zeroth-order data, we determine NEI model parameters for the regions which lead to density estimates. Values of $n_e \approx 100 \text{ cm}^{-3}$ are likely the maximum of a range of densities in this X-ray emitting material. The common "oxygen-rich" assumption is coarsely tested by comparing the integrated O VIII line flux and continuum levels. It appears that most of the continuum is due to another source, e.g., from He.

ABSTRACT

Chandra High-Energy Transmission Grating (HETG) X-ray spectra are extracted from 17 bright, narrow regions of Cas A and provide unique measurements of their kinematic and plasma states. From the dominant emission lines, e.g. He-like Si, we derive accurate Doppler shifts in the range -2500 to +4000 km s⁻¹; these agree well with transverse-velocity measurements and allow the features to be located in 3D. Plasma diagnostics of these regions indicate temperatures largely around 1 keV with some above 3 keV. Using as well the non-dispersed zeroth-order data, we determine NEI model parameters for the regions which lead to density estimates. Values of $n_e \approx 100 \, \mathrm{cm}^{-3}$ are likely the maximum of a range of densities in this X-ray emitting material. The common "oxygen-rich" assumption is coarsely tested by comparing the integrated O VIII line flux and continuum levels. It appears that most of the continuum is due to another source, e.g., from He.

Key Words: RADIATION MECHANISMS: THERMAL — SUPERNOVA REMNANTS: INDIVID-UAL(CAS A (G111.7–2.1)) — TECHNIQUES: SPECTROSCOPIC — X-RAYS: ISM

1. HETG OBSERVATION OF CAS A

The X-ray emitting material in young supernova remnants is the bulk of the ejected mass and gives direct information on the progenitor, the explosion mechanism, and illuminates the overall hydrodynamics at the present epoch. Cas A is a bright, Galactic remnant which allows detailed study in all wavebands. Here we add high spatial and spectral resolution X-ray measurements to the Cas A knowledge base.

The HETG is a slitless, dispersive spectrometer (Canizares et al. 2005)—nominally designed for point source observations. In contrast, Cas A is a very extended source compared to the HETG dispersion scale, Figure 1; the spacing between the bright Si dispersed images is not much larger than Cas A it-

self. Note that streaks of intensity variation are seen along the dispersed images, the most prominent low-intensity streaks form a wide "X" pattern³ and are likely due to a region of high local absorption (indicated on Fig. 7.)

In spite of Cas A's large size, we can obtain information from these dispersed data using general techniques as described in Dewey (2002). In particular, detailed analyses were carried out for Cas A's bright Si line emission and are presented in Lazendic et al. (2006), hereafter Paper I. In this present work we summarize those results in § 2 & § 3, and discuss further aspects in § 4 & § 5. Finally, future plans in these areas are discussed in § 6.

2. KNOT VELOCITIES

To the HETG, Cas A appears as a multitude of sources; for analysis, we selected 17 small, bright

¹MIT Kavli Institute, MIT Room NE80-6085, Cambridge, Massachusetts 02139, USA (dd@space.mit.edu).

 $^{^2{\}rm School}$ of Physics, University of Melbourne, Victoria 3010, Australia.

³These streaks were brought to our attention by Peter Ford of the ACIS science team—he initially feared that they may be instrumental in origin!

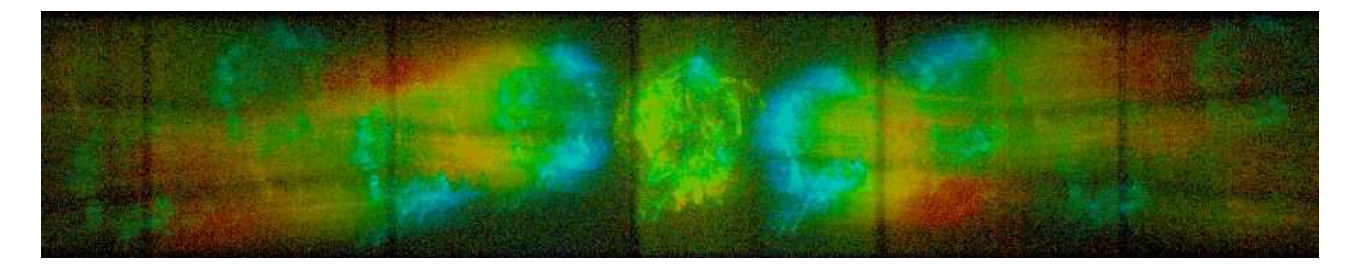


Fig. 1. Dispersed image of Cas A on the ACIS-S array. The undispersed "zeroth-order" image of Cas A is seen near the center; with axes roughly N to left and E down. Dispersed images of Cas A in the bright Si emission are visible to either side of the central image. The MEG spectrum extends from upper-left to lower-right and the HEG from lower-left to upper-right. Five vertical low-intensity regions indicate the gaps between the six ACIS CCD chips. The red-to-blue color range corresponds to 0.5 keV to 2.3 keV.

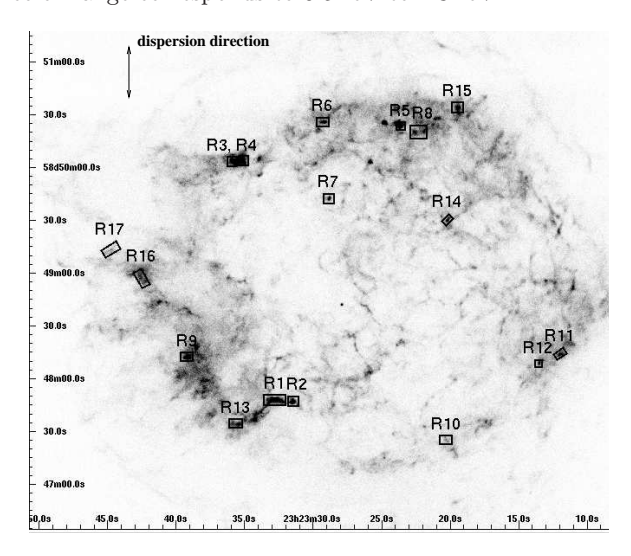


Fig. 2. The 17 regions are indicated on an X-ray image of Cas A (J2000 coordinates), from Lazendic et al. (2006).

knots (here, "knots" is used interchangeably with other terms: regions, features, filaments...), as indicated on Figure 2. We used the filament-analysis technique (Paper I) to narrow the features and increase the spectral resolution. The custom-created PHA and RMF files were then fit in ISIS (Houck 2002) to obtain line wavelengths and flux ratios.

Analysis of the line shifts of the bright He-like Si lines gives accurate Doppler velocities, in agreement with the transverse proper motions of DeLaney et al. (2004). Assuming a uniform-expansion velocity field, the regions can be assigned a line-of-sight z-coordinate: $z={\rm const}\times V_{\rm meas}$, and the regions can be located in 3D, as shown in Figure 3. The trend to blue-shifted velocities in the SE agrees qualitatively with early dispersive spectroscopy results (Markert et al. 1983).

3. PLASMA PROPERTIES

The f/r and H-like/He-like line ratios were used with an NEI-model-generated line-ratio grid to determine values of kT and ionization age, $\tau = n_e t$, for the regions studied. These values can be displayed on a "Laming plot", Figure 4. Note that unlike the knot series measured in Laming & Hwang (2003), the knots here were selected for their brightness and small size and so we don't expect them to trace out the full extent of a model curve but rather they should be located at the places of maximum Si-line emission along the model curves. The three high-temperature regions, R8, R10, and R17, clearly stand out from the general model expectations; R17 appears to be involved with the NE jet phenomenon, while R8 and R10 do not at first glance show a reason for their high temperatures.

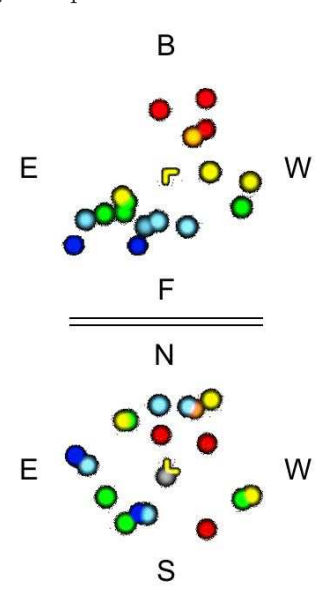


Fig. 3. The regions in 3D. Bottom: cartoon version of the regions on the sky. Top: the same regions viewed from "above" with the axes E–W and Front–Back indicated.

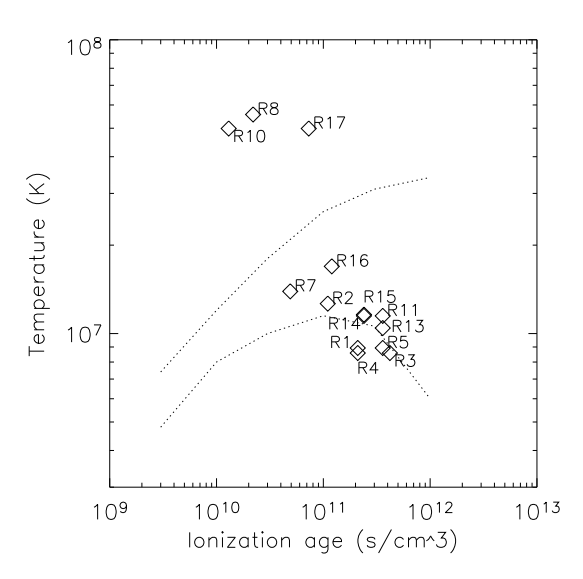


Fig. 4. Regions located in T vs. τ space; dotted lines indicate the min–max range of the model expectations shown in Laming & Hwang (2003).

Fixing the kT and τ values, we then fit the zeroth-order spectrum of each region in the range above 1.1 keV to determines the model "norm" and abundance values. The continuum in the model fitting was assumed to come from oxygen (Laming & Hwang 2003), see however the discussion in §5. Using a distance to Cas A of 3.4 kpc and estimated volumes for the regions, the NEI model values can be converted to densities of the ions and electrons in the regions (Paper I, Appendix B.)

The derived properties of these regions are plotted as a function of their 3D radius from the expansion center, Figure 5. There does not appear to be any clear trend of temperature or density with this radius as simple models (next section) might suggest. The two outer-most regions, R16 and R17, show solar-like abundances of Mg whereas the inner regions have Mg at generally sub-solar levels. In the plot of time-since-shocked, $t_{\rm shock} = \tau/n_e$, the backside regions closer to the center show lower values suggestive of their having more recently encountered the reverse shock (RS).

4. EJECTA DENSITY DISTRIBUTION

The ejecta densities of the measured regions are of order 100 cm⁻³; assuming this level is typical throughout the full 3D shell from 100" to 130" radius leads to a very large mass estimate of the continuum-providing oxygen (Paper I.) How do these inferred densities compare with expected densities and the generally assumed model picture?

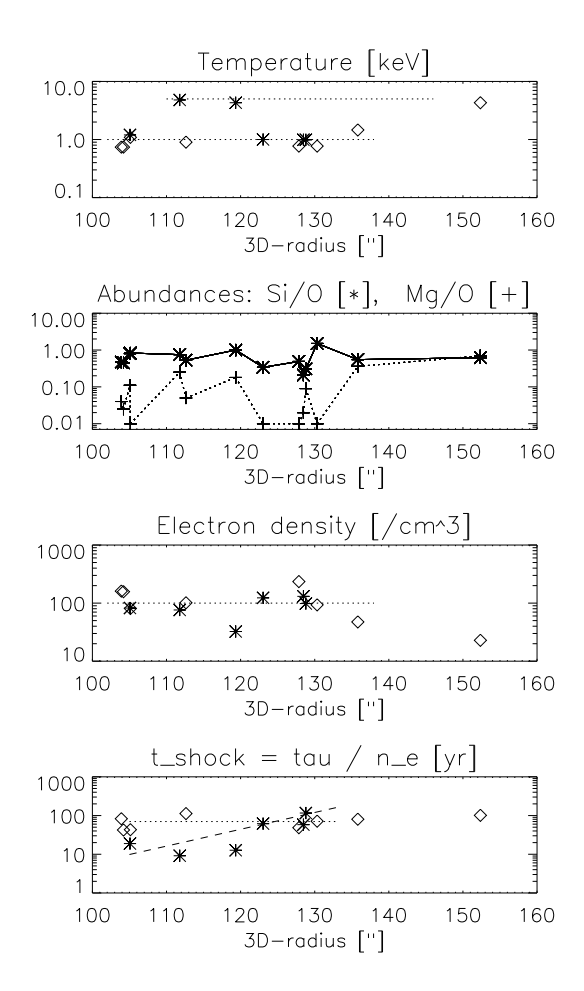


Fig. 5. Properties of the regions plotted vs. $r_{\rm 3D}$. Unless otherwise indicated, the "*" and diamond symbols correspond to regions on the back and front of the remnant, respectively. Lines on the plots serve to "guide the eye." (For clarity, the outlying region R17 is plotted at a radius of 152" instead of its actual value of 172".)

The high temperature X-ray gas should trace out the bulk hydrodynamics of the remnant, as opposed to the generally un-coupled optical FMKs and the more mysteriously coupled (magnetic fields and relativistic electrons) radio emission. The self-similar solution, e.g., Chevalier & Oishi (2003), for an s=2"wind" circumstellar medium shows a range of densities in the shocked ejecta with highest density at the contact discontinuity (CD, see their Figure 2.) Such a trend of density with radius is not seen in our data. However, as suggested by Laming (private communication), the radial location of the RS and CD may vary around the remnant and so the effective "thickness" of the high-density shell is much smaller than simply the range of radii over which we see high densities. Further, it is likely that Rayleigh-Taylor (R-T) instabilities will distort the otherwise sharp CD (Chevalier et al. 1992; Dwarkadas 2000); note that even with R-T effects a similarly large range of ejecta densities may still be maintained, Figure 6. The bright, dense regions measured here then reflect the higher-density portions of the hydro structures developed by the ejecta between the RS and CD. Extrapolating from their density values to an overall mass estimate requires further assumptions of the underlying density distribution.

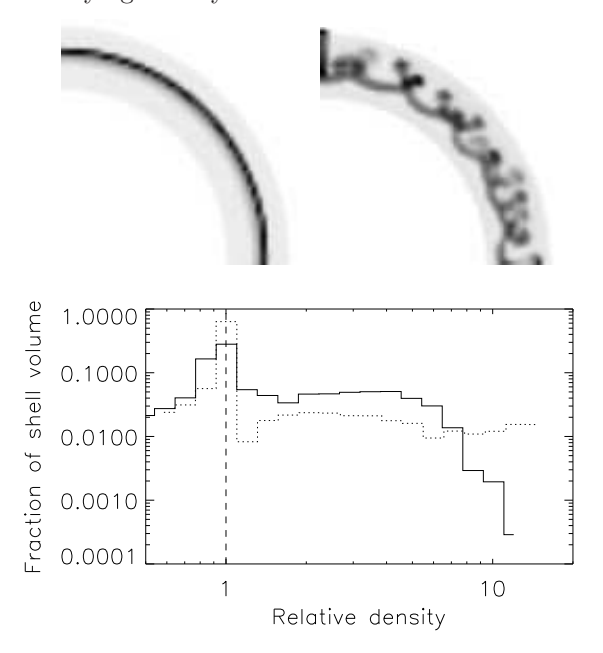


Fig. 6. Histograms of model ejecta densities. The images at upper left and right show cross-sections of a simple self-similar distribution and an R-T-hydro density distribution, respectively. Histograms of the densities in a 3D shell from these models are plotted below; the R-T-hydro simulation is the solid line. Both models show a range of densities extending to 10 or more times the most common value.

5. OXYGEN-RICH?

It has been noted that bright ejecta-dominated regions of Cas A cannot be modeled with a pure high-Z metals plasma due to a need for additional continuum flux from elements with "Z < 8" (Hughes et al. 2000). The continuum could arise from mixed-in outerlayer material: He, N, perhaps C (Pérez-Rendón et al. 2002). In Laming & Hwang (2003) and our Paper I this continuum was assumed to come from oxygen for modeling purposes.

One reason that the actual amount of oxygen is an unsettled issue is that Cas A is strongly absorbed with an $N_{\rm H}$ of order of $10^{22}\,{\rm cm}^{-2}$, greatly reducing the O VIII emission. Even so, the ACIS imaging data does include oxygen-band emission which

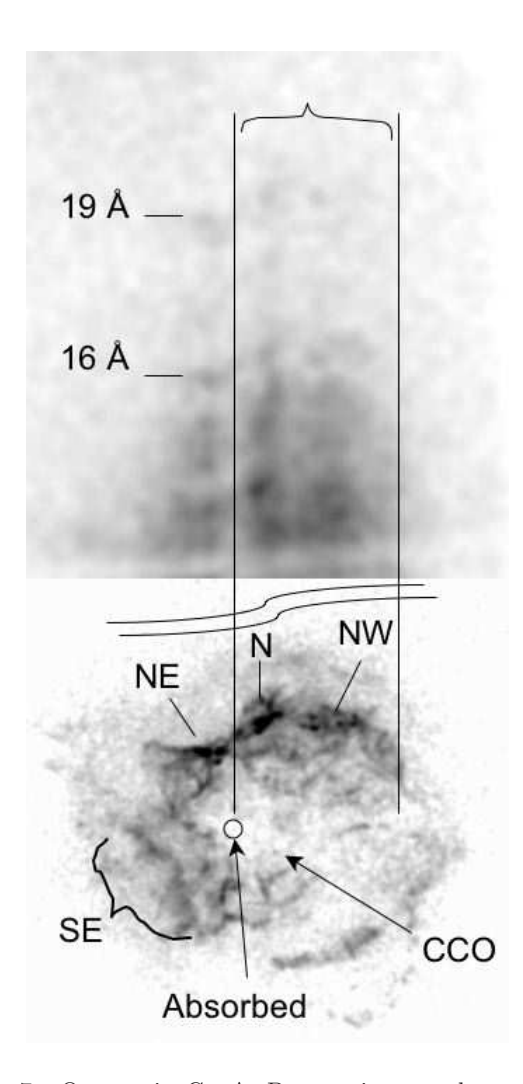


Fig. 7. Oxygen in Cas A. Bottom image: the oxygen band, $0.5\,\mathrm{keV}$ to $0.8\,\mathrm{keV}$, from the non-grating observation, obsid 5196. The main O-bright regions are labeled. Upper image: the MEG-dispersed events on S1 (binned and smoothed) from obsid 1046; discrete O VIII line emission is just visible from portions of the NE, N, and NW regions. Vertical lines indicate the extraction region for the spectrum of Figure 8.

shows greatest intensity in four general regions: labeled NE, N, NW and SE in the bottom image of Figure 7.

It is possible to look for and set limits on the oxygen emission using the OVIII Ly α and Ly β lines seen in the MEG spectrum of Cas A; these lines were also measured with the XMM-Newton RGS (Bleeker et al. 2001). In that work the L α -to-L β ratio was measured versus cross-dispersion location, separating the SE, NE, N regions. We defer a similar detailed analysis and instead consider here the global spectrum from the combined N & NW region.

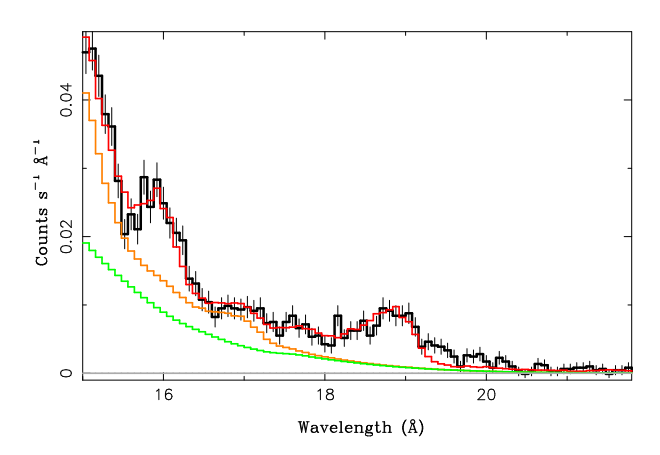


Fig. 8. Oxygen seen with the MEG. The histogram extracted from the extended N&NW region is well-fit by a set of XSPEC vnei models which include He, Fe, and O. The underlying He and He+Fe components are also shown; the model is for the $kT=0.7\,\mathrm{keV}$ and $\tau=0.2\times10^{11}\,\mathrm{s\,cm^{-3}}$ case of Table 1.

The extracted counts spectrum using our filament technique is shown in Figure 8. This spectrum is fit by an absorbed vnei model containing only He, Fe, and O. The observed lines are broader than the spatial image and velocity components of $+1500\,\mathrm{km\,s^{-1}}$ and $-2100\,\mathrm{km\,s^{-1}}$ are included. The difficulty of working in this heavily absorbed range with relatively low resolution data is demonstrated by the fitting results given in Table 1. The table shows that comparably good fits can be obtained over a large (but relevant) range of kT and τ , hence, the data really constrain only four of the six model parameters. Note that $N_{\rm H}$ is considered a free parameter here both for illustration of its effect on the fit parameters and to allow the possibility that it differs from the expected range of $1.0-1.2\times10^{22}\,\mathrm{cm^{-2}}$ (Keohane et al. 1996).

Even with this degeneracy some preliminary conclusions are possible: i) the integrated Fe/O abundance ratio is greater than 0.2 solar and ii) there is substantial He (and/or C, N) compared to O+Fe, with $M({\rm O+Fe})<0.01\,M({\rm He})$. We can conclude that Cas A is dominated by O burning products (Si, S, etc.) rather than by oxygen per se.

As a caveat, note that given the large region extracted and the unavoidable inclusion of a large radial range, which includes the blastwave, it is possible that a finite contribution to the measured continuum comes from synchrotron radiation (Hughes et al. 2000).

6. FUTURE WORK

The current HETG data has produce a small but tantalizing set of measurements on bright knots in Cas A and given some information on the oxygen present in the remnant. Some additional work in these directions is listed here:

- It should be possible to measure the Doppler shifts of additional knots in this data set as well as study individual bright oxygen features.
- We can compare the (sparse) 3D X-ray structure here with the optical/IR "ring" structures (Reed et al. (1995) and unpublished additional work.)
- We have not yet examined the dispersed Fe-K emission in this data to see if it contains useful information; if the Fe is indeed in fuzzy bubbles then our slitless dispersive data will have reduced spectral resolving power.
- The non-dispersed *Chandra* 1 Ms data set is a unique resource and these grating results can be used to confirm/calibrate the CCD-measured Doppler shifts.
- It will be useful to create a "Cas A knot catalog" to allow comparisons across analyses, wavelengths, and epochs.
- Although Suzaku lacks the spatial resolution to isolate individual knots, it does have better energy resolution in the oxygen band and may help constrain global Cas A emission models.
- X-ray features in Cas A are changing in time (Patnaude & Fesen 2006) and a future HETG re-observation ($\Delta t > 6$ years) could give useful information on knot evolution.

In the modeling domain, the analyses presented here suggest a larger goal of building an approximate 3D model of the Cas A remnant (at a given epoch) from a set of physically-consistent emission components. Work with this flavor is already underway in astrophysics, e.g., in the modeling of planetary nebulae (Morisset et al. 2005; Steffen & López 2006), and will be accelerated by making more use of the 3D capabilities of current computer hardware and software.

Finally, in the more distant hardware future, one might imagine a "soft X-ray spectrometer" with a long-slit configuration operating in this low-energy range⁴ to better isolate and measure the emission from complex extended sources like Cas A.

 $^{^4\}mathrm{A}$ minimum range of 14.5 Å to 22.5 Å would include important Fe-L and O lines. Extending shortward to include Ne X (12 Å) and/or longward to include C and N lines (26-30-35-42 Å), would of course be desirable.

Fixed Values		Fit Parameters					Derived Values ^c		
kT (keV)	τ (10 ¹¹ s cm ⁻³)	$N_{\rm H}$ $(10^{22}{\rm cm}^{-2})$	Fe/O	О/Не	$X_{\text{norm}}^{\text{b}}$ (10^{-3})	χ^2	$\frac{n_e}{(\text{cm}^{-3})}$	$M_{ m He}$ $(M_{ m solar})$	τ/n_e (years)
0.7	0.16	1.05	0.38	0.017	18.1	1.18	73.	11.2	6.9
0.7	0.20	1.0	0.46	0.016	14.5	1.11	65.	10.0	9.7
0.7	0.30	0.9	0.68	0.013	9.9	1.08	54.	8.3	17.
0.7	0.60	0.8	0.82	0.013	7.0	1.10	45.	7.0	42.
0.7	1.30	0.7	0.53	0.031	4.8	1.08	38.	5.8	109.
0.7	3.00	0.7	0.15	0.154	4.3	1.05	36.	5.4	266.
0.9	0.20	0.9	0.69	0.012	8.6	1.08	50.	7.7	12.5
0.9	0.60	0.6	1.98	0.014	2.2	1.04	25.	3.9	74.
0.9	3.00	0.4	0.64	0.234	0.78	0.93	15.	2.3	623.
1.2	0.16	0.8	1.03	0.010	5.0	1.07	38.	5.9	13.1
1.2	0.60	0.4	4.87	0.016	0.74	0.94	15.	2.3	128.
1.2	3.00	0.6	0.69	0.290	2.9	1.04	29.	4.4	323.

TABLE 1 MODEL^a FITS TO THE OXYGEN AND FE-L EMISSION FROM THE N & NW REGION

In all this we are guided by our current theories, but the data have the last word and there may well be some "non-spherical-elephant" surprises along the way.

We thank Claude R. Canizares for providing GTO time for this observation and Vikram Dwarkadas for providing 2D R-T data. Thanks to Martin Laming and Rob Fesen for useful conversations. Support for this work was provided by NASA/USA through the Smithsonian Astrophysical Observatory (SAO) contract SV3-73016 to MIT for Support of the *Chandra* X-Ray Center, which is operated by the SAO for and on behalf of NASA under contract NAS8-03060.

REFERENCES

Bleeker, J. A. M., Willingale, R., van der Heyden, K., Dennerl, K., Kaastra, J. S., Aschenbach, B., & Vink, J. 2001, A&A, 365, L225

Canizares, C. R., et al. 2005, PASP, 117, 1144

Chevalier, R. A., Blondin, J. M., & Emmering, R. T. 1992, ApJ, 392, 118

Chevalier, R. A., & Oishi, J. 2003, ApJ, 593, L23

DeLaney, T., Rudnick, L., Fesen, R. A., Jones, T. W., Petre, R., & Morse, J. A. 2004, ApJ, 613, 343 Dewey, D. 2002, High Resolution X-ray Spectroscopy with XMM-Newton and Chandra, 14D (ADS)

Dwarkadas, V. V. 2000, ApJ, 541, 418

Houck, J. C. 2002, High Resolution X-ray Spectroscopy with XMM-Newton and Chandra, 17H (ADS)

Hughes, J. P., Rakowski, C. E., Burrows, D. N., & Slane, P. O. 2000, ApJ, 528, L109

Keohane, J. W., Rudnick, L., & Anderson, M. C. 1996, ApJ, 466, 309

Laming, J. M., & Hwang, U. 2003, ApJ, 597, 347

Lazendic, J. S., Dewey, D., Schulz, N. S., & Canizares, C. R. 2006, ApJ, 651, 250 (Paper I)

Markert, T. H., Clark, G. W., Winkler, P. F., & Canizares, C. R. 1983, ApJ, 268, 134

Morisset, C., Stasińska, G., & Peña, M. 2005, MNRAS, 360, 499

Patnaude, D. J., & Fesen, R. A. 2006, AJ, accepted; astro-ph/0609412

Pérez-Rendón, B., García-Segura, G., & Langer, N. 2002, RevMexAA, 12, 94

Reed, J. E., Hester, J. J., Fabian, A. C., & Winkler, P. F. 1995, ApJ, 440, 706

Steffen, W., & López, J. A. 2006, RevMexAA CS, 26, 30

^aThe model is an XSPEC wabs*vnei with kT and τ fixed as tabulated. The elemental abundances are: H=1, He=1000, O and Fe are free, and all others are set to 0.0.

^bX_{norm} is the usual XSPEC model "norm" value; see Paper I Appendix B for details.

^cThese physical parameters are based on an emitting volume equal to the cross-dispersion width (128") times one quadrant of the annulus from 100" to 130": $V = 0.25*128*\pi(130^2-100^2) \approx 9.3\times10^{55} \,\mathrm{cm}^3$. The equations of Paper I Appendix B are used with a distance to Cas A of 3.4 kpc.